ARL-TR-9866 • JAN 2024

DEVCOM ARMY RESEARCH LABORATORY

Modeling Dynamic Uniaxial Compression of a Ferrous Alloy in an External Magnetic Field

by John D Clayton

NOTICES

Disclaimers

The findings in this report are not to be construed as an official Department of the Army position unless so designated by other authorized documents.

Citation of manufacturer's or trade names does not constitute an official endorsement or approval of the use thereof.

Destroy this report when it is no longer needed. Do not return it to the originator.

ARL-TR-9866 ● JAN 2024

Modeling Dynamic Uniaxial Compression of a Ferrous Alloy in an External Magnetic Field

John D Clayton
DEVCOM Army Research Laboratory

REPORT DOCUMENTATION PAGE

1. REPORT DATE	2. REPORT TYPE	3. DATES COVERED	
		START DATE	END DATE
January 2024	Technical Report	10/1/2023	12/12/2023

4. TITLE AND SUBTITLE

Modeling Dynamic Uniaxial Compression of a Ferrous Alloy in an External Magnetic Field

5a. CONTRACT NUMBER	5b. GRANT NUMBER	5c. PROGRAM ELEMENT NUMBER
5d. PROJECT NUMBER	**5e. TASK NUMBER**	**5f. WORK UNIT NUMBER**

6. AUTHOR(S)

John D Clayton

7. PERFORMING ORGANIZATION NAME(S) AND ADDRESS(ES)

DEVCOM Army Research Laboratory
ATTN: FCDD-RLA-TB
Aberdeen Proving Ground, MD 21005-5066

8. PERFORMING ORGANIZATION REPORT NUMBER

ARL-TR-9866

9. SPONSORING/MONITORING AGENCY NAME(S) AND ADDRESS(ES)	10. SPONSOR/MONITOR'S ACRONYM(S)	11. SPONSOR/MONITOR'S REPORT NUMBER(S)

12. DISTRIBUTION/AVAILABILITY STATEMENT

Approved for public release; distribution is unlimited.

13. SUPPLEMENTARY NOTES

primary author's email: <john.d.clayton1.civ@army.mil>
ORCID ID: John D Clayton 0000-0003-4107-6282

14. ABSTRACT

Modeling of dynamic compression of a ferrous alloy with ferromagnetic and weakly paramagnetic phases is undertaken. The constitutive model, published in prior works by the author and collaborators, includes finite strains, nonlinear thermoelasticity, rate-dependent plasticity, and solid-solid phase transformations. Maxwell's equations for conductors use a quasi-magnetostatic approximation. The present calculations treat a material element as an isotropic mixture of coexisting phases. Deformations and magnetic field are locally homogeneous over phases, but magnetization is not. Phase transition kinetics account for effects of magnetic fields. Previously determined phase transition parameters were obtained for this alloy under mechanically quasi-static, tensile loading. Here, predictions are obtained with these parameters, and with those of pure iron, for boundary conditions mimicking those witnessed in plate impact experiments. Effects of external magnetic fields of strength 2 T on the stress-volume response are predicted to be small. Transition initiation pressures, in contrast, are notably affected by such fields. Different parameter choices impede or promote transitions. Hugoniot predictions are similar to existing data on stainless steels.

15. SUBJECT TERMS

ferrous metals, equation of state, plasticity, phase transitions, damage, magnetohydrodynamics, Terminal Effects

16. SECURITY CLASSIFICATION OF:			17. LIMITATION OF ABSTRACT	18. NUMBER OF PAGES
a. REPORT	b. ABSTRACT	C. THIS PAGE		
UNCLASSIFIED	UNCLASSIFIED	UNCLASSIFIED	UU	43

19a. NAME OF RESPONSIBLE PERSON	19b. PHONE NUMBER *(Include area code)*
John D Clayton	410-278-6146

STANDARD FORM 298 (REV. 5/2020)
Prescribed by ANSI Std. Z39.18

Contents

List of Figures

List of Tables

Acknowledgments

The author acknowledges support from the US Army Combat Capabilities Development Command (DEVCOM) Army Research Laboratory (ARL).

Dr Matt Coppinger (Applied Physics Branch, ARL) is thanked for helpful discussion on recent experiments at ARL of impact-induced shock compression of ferrous alloys under external magnetic fields.

1. Introduction

Magnetic fields can influence phase transformations in ferrous materials. External fields alter the Gibbs free energy difference between phases with different magnetic properties, for example, ferromagnetic versus paramagnetic phases. As a result, the solid-solid phase transformation barrier and transition kinetics change when the external field strength changes. This phenomenon is documented in experiments on pure iron (Fe) and various steels, whereby, for example, $\alpha \leftrightarrow \gamma$ transformation temperatures are affected by external magnetic fields.[1,2] In ferrous alloys of present interest, the body-centered cubic (BCC) α phase is typically ferromagnetic and of lower ambient mass density than the weakly magnetic close-packed phases: the face-centered cubic (FCC) γ phase and the hexagonal close-packed (HCP) ϵ phase. The pressure-temperature phase diagram of pure Fe at null applied magnetic field is well known,[3–5] where α is favored at low temperatures and pressures, γ at high temperatures, and ϵ at high pressures. Effects of external magnetic fields on phase transitions at high pressures have witnessed few experimental studies[3,6] and are less well-understood theoretically, though notable progress has recently been made.[7]

Magnetically influenced transformations in Fe and Fe-based alloys have been studied using thermodynamic theory[8] and phase-field simulations.[9] At the scale of microstructure, phase-field simulations have been used to study domain evolution in ferromagnetic crystals.[10–12] Magnetic fields may also affect ductility and fracture of steels.[13,14] Plastic flow from dislocation slip and twinning could likewise be affected by electromagnetism, as documented for various crystalline solids[15–17] and predicted from a continuum theory of magnetic single crystals.[18]

The present work invokes a macroscopic model for the polycrystalline response, whereby each continuum point consists of numerous crystals of various orientations, and whereby such crystals comprise multiple solid phases in locally mixed-phase regions. At comparable length scales, continuum phase transformation models for Fe and steels include several for quasi-static loading[19,20] and more recent formulations[5,21,22] for dynamic loading. The polycrystal model of Clayton and Lloyd[21] was used to capture behaviors of three different medium-high Mn-alloy steels dominated by slip, twinning, or phase transitions depending on composition, applied stress state, and temperature. That model,[21] unlike a predecessor implemented by Boettger and Wallace,[5] permits a shear driving force in transformation kinetics, as

well as ductile damage leading to failure. However, only one-way transformations are modeled in that study[21] under a kinetic law similar to one used by Turteltaub and Suiker[23] for anisotropic single crystals. None of the aforementioned theories[5,19–23] accounted for effects of applied electromagnetic fields.

A continuum mechanical model with electromagnetic coupling has recently been formulated and implemented for simulation and analysis of magnetizable polycrystalline solids under finite deformations.[7,24,25] Exchange effects are not explicitly included in the macroscopic description, however, as likewise omitted in other papers[26–28] and Chapter 3 of the book by Maugin.[29] No separate balance law for electronic spin is required, nor are gradients of magnetization included in the free energy. In contrast, another recent theory[30] omits inelasticity and dynamics but features a more intricate differential-geometric treatment of nonlinear elasticity coupled to magnetization in saturated ferromagnets, including a balance for electronic spin angular momentum.[31] Origins and interpretations of the Maxwell stress tensor entering pertinent continuum mechanical theories with electromagnetic field effects (e.g., those cited above) have been scrutinized elsewhere.[32]

Alternative models of finite-strain continuum mechanics accounting for coupled elastic, plastic, thermal, and structural transformation physics exist,[33] with a few also including magnetic-field influences on phase transitions in shape memory alloys.[34] The latter class of materials has also been analyzed and numerically simulated at the scale of discrete twins and magnetic domains.[35] This scale is smaller than that resolved by the isotropic polycrystal model implemented herein.

Alloying of Fe with other elements can drastically affect free energy differences between solid phases and thus alter transformation stresses and temperatures.[1,2,8,36] Phase transitions can be beneficial to strength and ductility. For example, consider transformation-induced plasticity (TRIP), whereby to accommodate deformation from transformation, regions surrounding the transformed material deform plastically.[19,20,23] The transformation and plastic deformations contribute ductility, while the transformed martensitic phase contributes higher hardness and strength than the parent austenite phase. Alloying affects the stacking fault energy, for which a lower value is usually associated with a greater tendency to transform[19,37] (i.e., a lower transformation stress).

A recent study[7] modeled behaviors of two novel ferrous alloys developed at the

US Army Combat Capabilities Development Command (DEVCOM) Army Research Laboratory (ARL). The shared composition of these alloys includes significant chromium (Cr), Manganese (Mn), and nickel (Ni). Alloys were subjected to one of two different processing routes (i.e., different heat treatments), leading to an as-rolled (AR) versus heat-treated (HT) designation scheme for the material. Heat treatment furnishes a different starting microstructure for the HT material that influences kinetic factors of phase transformations rather than thermodynamics, in the sense that free energy of pure phases (excluding defects) depends only on chemical composition for a given stress-temperature-magnetic field state. However, phase diagrams accounting for composition, temperature, pressure, and magnetic field are not presently available from experiments or calculations for this complex alloy system. Quasi-static tensile experiments revealed that a magnetic field on the order of 1 T affected transformations and tensile stress-strain response for these two alloys. A dominant influence of magnetic field on martensitic transition kinetic parameters for pure Fe and the two alloys, as discovered in that investigation,[7] was observed in earlier experiments and modeling of a different maraging steel.[36]

Problems solved in the current application to ferrous alloys are too complex to enable analytical solutions, even for uniaxial-strain loading. Coupled plasticity and transformation behaviors, with or without electromagnetic effects, require numerical schemes that exceed prior analytical (albeit still iterative) methods[24] that were feasible only under assumptions of constant flow stress and negligible effects of shear on transition kinetics. These simplifying assumptions were acceptable only for pure Fe in hydrostatic compression and in the planar shock compression regime. Strength effects are small relative to transition pressures in pure Fe, and shear does not seem to affect transition thresholds between α and ϵ phases in pure Fe.[3–5,38]

In tensile testing conditions, the pressure and stress deviator are of comparable magnitude, so a more realistic strength model for ferrous alloys with evolving flow stress is required. Effects of shear on transformation in the class of austenitic-martensitic alloys are expected to be substantial.[21] Even in pure Fe, transition driving forces could be influenced by shear under non-shock conditions.[39,40] These effects were newly incorporated in the constitutive models and numerical approaches developed in the author's most recent works[7,25] that consistently couple electromagnetic and mechanical phenomena. Importantly, the most recent theory and numerical implementation[7,25] enables kinetic parameters for phase transitions to depend on the lo-

cal magnetic field strength. Such dependence was found crucial for modeling the influence of external fields on transformation behaviors of pure Fe under shock compression[3] and the novel ARL-designed alloys under quasi-static extension.[7]

In prior theory,[24] a multiplicative decomposition of the deformation gradient into distinct terms for plasticity, twinning, transformation, and damage (e.g., in the form of void growth) was invoked. Finite volumetric and deviatoric elastic strains were used in all constitutive descriptions and problem solutions. These physically precise practices were manageable for the reduced-dimensionality problems solved analytically therein, again under assumptions of constant flow stress and null transformation shear. For more challenging 2-D and 3-D problems, further idealizations[7,25] are required for computational efficiency within the scope of contemporary, coupled solid mechanics and magnetohydrodynamics solvers (e.g., simulation codes `ALEGRA`[41] and `ALE3D`[42]). Suitability of these idealizations and accuracy of numerical methods were verified in two recent works.[7,25] The software manual in a recent report[25] describes several model frameworks; the present formulation is referred to as constitutive model framework 1 (CMF1) in that report. CMF2 of that report[25] corresponds to the formulation of Clayton and Lloyd[21] that excludes magnetism and is not used herein.

Recent experiments (unpublished) at ARL subjected samples of the alloy to dynamic impact loading under external magnetic fields of strength up to approximately 2 T. Approximate peak impact stresses approached 10 GPa. Magnetic fields were aligned parallel to the direction of impact and parallel to the direction of compressive strain. Experimental data suggested substantial influences of external fields on free surface velocity profiles. Data were inconclusive, with substantial variability, so more experiments are in progress that would support definitive conclusions. The objective of the present study is application of the theoretical-computational framework of Clayton et al.[7,25] to model the response of an element of material under conditions that closely approximate those witnessed in these recent experiments.

The present study only models the AR alloy. Modeling the dynamic compressive response of the HT alloy, the material of focus of initial experiments, will be reported in the future, likely in conjunction with existing and forthcoming data from those experiments and microstructure characterization. Results in the present re-

port, combined with the future calculations, will also support comparison of the predicted responses after different heat treatments.

Under compressive loading, the material should presumably transform from its less dense phase (i.e., BCC α) to its more dense phase(s) (i.e., FCC/HCP γ/ϵ). In contrast, under quasi-static tensile loading, the material transformed in the opposite direction[7,25]: $\gamma/\epsilon \rightarrow \alpha$. Transition kinetic parameters were calibrated for the AR alloy only for the latter direction, under isothermal conditions at room temperature, in prior work.[7] Since kinetic parameters are unknown a priori for the former low-to-high density transformation in the AR alloy, two assumptions are considered in the present modeling investigation. In the first, the kinetic parameters calibrated for quasi-static tensile transformation of the AR alloy are applied to the reverse transition of the same alloy under adiabatic compression. In the second, the kinetic parameters for the $\alpha \rightarrow \epsilon$ adiabatic compression of pure Fe[7] are applied for the $\alpha \rightarrow \gamma/\epsilon$ transition of the AR alloy. Ramifications of each assumption on transition initiation stresses are evaluated using the model, with and without applied magnetic fields of strength 2 T. External fields aligned parallel (as in the experiments) and perpendicular to the impact direction are both analyzed in simulations to quantify differences in transition thresholds.

Remaining sections of this report are organized as follows. Section 2 gives an overview of the theoretical model and numerical implementation. This content briefly summarizes prior publications,[7,24,25] augmented with clarifications not included in prior work. Section 3 describes the simulation protocols including model parameters. Section 4 analyzes the results. Section 5 gives the conclusions.

A list of acronyms and notation follows the list of works cited. The former list is representative but not comprehensive since the full set of mathematical variables from past publications on the theory and numerical methods[7,24,25] is prohibitively large. The present notation follows that of these recent related works[7,24,25] to which the reader is referred.

2. Constitutive Model Summary

The theory and numerical implementation comprise a complex, multi-physics framework. As with most sophisticated frameworks in nonlinear continuum mechanics, whether or not a unique, physically valid solution exists for a given problem depends on the material properties and imposed initial and boundary conditions. The current model and numerical algorithms have been verified[7,25] to give stable, physically credible solutions for the material properties and loading conditions as compared with experimental data in those works.

The complete set of equations and algorithms is too lengthy to present in the current report. Details necessary for understanding problems addressed in Section 3 are described in Section 2.1: the original constitutive model for phase transformations[24] and its more recent generalization to include magnetic field effects.[7] Requisite features of the composite deviatoric flow model[21] generalized to include magnetic field effects[7] are also discussed. Subsections 2.2, 2.3, and 2.4 discuss features of the model and comparisons with alternative approaches from the literature. This content is new and was too long to include in past publications.[7,24,25] These subsections, though relevant for interpretation of the constitutive model, can be bypassed if the reader is only interested in the results of simulations discussed in Sections 3 and 4.

2.1 Magnetically Influenced Phase Transformations and Deviatoric Flow

Denote the volume fraction of the transformed phase by ξ. To ensure non-negative net dissipation from the transformation rate $\dot{\xi}$, the kinetic law for transitions is required to satisfy[7,24,25]

$$\mathfrak{D}^{\xi} = -\Delta^{*}\mathbb{G} \cdot \dot{\xi} \geq 0. \tag{1}$$

The total Gibbs free energy difference, specifically the local energy density of the potentially transformed phase (1) minus that of the initial phase (0), is $\Delta^{*}\mathbb{G} = \mathbb{G}^{(1)} - \mathbb{G}^{(0)}$. For forward transitions, $\dot{\xi} > 0$ necessitates that the Gibbs free energy must not increase: $-\Delta^{*}\mathbb{G} \geq 0 \Leftrightarrow \mathbb{G}^{(1)} \leq \mathbb{G}^{(0)}$. Similarly, to ensure thermodynamically neutral or dissipative reverse transformations, the local Gibbs free energy density must not increase, where signs of $\Delta^{*}\mathbb{G}$ and $\dot{\xi}$ are reversed.

The theory of Boettger and Wallace[5] and Lloyd et al.[22] is enriched in recent works[7,24] to allow $\Delta^{*}\mathbb{G}$ to depend on shear (i.e., deviatoric) stress, magnetic flux density, and other state variables. These dependencies enlarge the classical pressure and tem-

perature dependencies of $\mathbb{G}^{(\alpha)}$ used in prior theory.[5,22] The local metastable state value of ξ, written $\xi^m(\boldsymbol{X},t)$, is obtained from $\mathrm{d}\xi = (1-\xi)\mathrm{d}\bar{\mathbb{F}}$, where the dimensionless forward transition driving force is $\bar{\mathbb{F}} = -\Delta^*\mathbb{G}/\beta^F$. Proportionality factor β^F for forward transformation can depend on the local thermodynamic and magnetic state, as can the activation energy barrier α^F. Conditions $\alpha_0^F/\beta_0^F = \alpha^F/\beta^F$ are prescribed so integration produces a metastable volume fraction ξ^m:

$$\int_0^{\xi^m} \frac{\mathrm{d}\xi}{1-\xi} = \int_{\alpha_0^F/\beta_0^F}^{-\Delta^*\mathbb{G}/\beta^F} \mathrm{d}\bar{\mathbb{F}} \quad \Rightarrow \quad \xi^m(\boldsymbol{X},t) = 1 - \exp\left[\frac{\alpha^F + \Delta^*\mathbb{G}(\boldsymbol{X},t)}{\beta^F}\right]. \tag{2}$$

The trial $(\cdot)^t$ forward transformation rate is given by linear relaxation kinetics[5,43]:

$$-\Delta^*\mathbb{G} > \alpha^F \text{ and } \xi(\boldsymbol{X},t) < \xi^m(\boldsymbol{X},t) \quad \mapsto \quad \dot{\xi}^t = (\xi^m - \xi)/\tau^F > 0, \tag{3}$$

with $\tau^F > 0$ a scalar having dimensions of time. Metastable states correspond to the limiting condition $\tau^F \to 0$. For finite τ^F, metastable equilibrium is attained for long time increments $\Delta t \gg \tau_F$ as arising for slowly varying transient solutions.

In reverse transformations, $\dot{\xi}^t < 0$ and $\mathrm{d}\xi = -\xi\mathrm{d}\bar{\mathbb{F}}$ with $\bar{\mathbb{F}} = \Delta^*\mathbb{G}/\beta^R$. Let β^R and α^R be the proportionality constant and activation energy barrier for reverse transitions with $\alpha_0^R/\beta_0^R = \alpha^R/\beta^R$ and $\tau^R > 0$ the time scale for kinetics. Then

$$\int_{\xi^m}^0 \frac{\mathrm{d}\xi}{\xi} = -\int_{\Delta^*\mathbb{G}/\beta^R}^{\alpha_0^R/\beta_0^R} \mathrm{d}\bar{\mathbb{F}} \quad \Rightarrow \quad \xi^m(\boldsymbol{X},t) = \exp\left[\frac{\alpha^R - \Delta^*\mathbb{G}(\boldsymbol{X},t)}{\beta^R}\right]; \tag{4}$$

$$\Delta^*\mathbb{G} > \alpha^R \text{ and } \xi(\boldsymbol{X},t) > \xi^m(\boldsymbol{X},t) \quad \mapsto \quad \dot{\xi}^t = (\xi^m - \xi)/\tau^R < 0. \tag{5}$$

When conditions contrary to Eqs. 3 and 5 hold, no transformation is possible:

$$\left.\begin{array}{ll} -\ \alpha^F \le \Delta^*\mathbb{G} \le \alpha^R & \text{and/or} \\ -\ \Delta^*\mathbb{G} < \alpha^F \text{ and } \xi > \xi^m & \text{or} \\ \quad \Delta^*\mathbb{G} > \alpha^R \text{ and } \xi < \xi^m & \end{array}\right\} \mapsto \dot{\xi} = \dot{\xi}^t = 0. \tag{6}$$

Quantities $\alpha^F, \alpha^R, \beta^F, \beta^R, \tau^F$, and τ^R can all potentially depend on local material state in the novel theory.[7] However, in the current software implementation,[25] τ^F and τ^R are fixed constants, and the phase transition barriers $\alpha^F, \alpha^R, \beta^F$, and β^R are

permitted to depend only on local magnetic field strength $|\boldsymbol{H}|$ in a linear manner:

$$\alpha^{F/R} = \alpha_0^{F/R} + \alpha_1^{F/R}\mu_0|\boldsymbol{H}|, \qquad \beta^{F/R} = \beta_0^{F/R} + \beta_1^{F/R}\mu_0|\boldsymbol{H}|. \tag{7}$$

Eight material constants are $\alpha_0^{F/R}, \alpha_1^{F/R}, \beta_0^{F/R}$, and $\beta_1^{F/R}$. In a recent report,[25] the linear $|\boldsymbol{H}|$-field dependence is assumed identical for forward and reverse metastable states, though this is not essential. Generally, α^F and α^R are unrestricted in sign, but $-\alpha^F \leq \alpha^R$, $\beta^F > 0$, and $\beta^R > 0$ are physical restrictions.

The transformation driving force $\Delta^*\mathbb{G}$ is divided into mechanical (i.e., pressure and shear), magnetostatic, and chemical (i.e., compositional and thermal) contributions:

$$\begin{aligned}
\Delta^*\mathbb{G} &= \Delta^*\hat{\mathbb{G}} + \Delta^*\tilde{\mathbb{G}} + \Delta^*\bar{\mathbb{G}} && \text{(total)},\\
\Delta^*\hat{\mathbb{G}} &= pJ\delta^{\xi}/[1 + (\xi - \xi_0)\delta^{\xi}] - \sqrt{\tfrac{1}{6}}J\bar{\sigma}^V\gamma^{\xi} && \text{(mechanical)},\\
\Delta^*\tilde{\mathbb{G}} &= \Delta^*\Phi && \text{(magnetostatic)},\\
\Delta^*\bar{\mathbb{G}} &= -\Delta^*A[\mathsf{B}_0 \ln J^E\Delta\theta] - \Delta^*\hat{c}_V[\theta\ln(\theta/\theta_0) - \Delta\theta]\\
&\qquad - (\lambda_T/\theta_T)(\theta - \theta_T) + \psi_0 && \text{(chemical)}.
\end{aligned} \tag{8}$$

The Jacobian determinant of the deformation gradient is J, and J^E is the thermoelastic part of J. The difference in thermal expansion coefficients (transformed phase minus initial phase) is $\Delta^*A = A^{(1)} - A^{(0)}$, with $A^{(\alpha)}$ the volumetric coefficient of thermal expansion of phase α, treated as a constant. The magnetic field-independent part of specific heat is $\hat{c}_V$. The latent heat coefficient of transformation is λ_T, and θ_T is a material constant called the transformation temperature. Energy density ψ_0 is the free energy of the transformed phase relative to the free energy of the initial phase at reference temperature θ_0, at null lattice deformation (i.e., at no mechanical or thermal loads) and at null applied magnetic field. See Clayton et al.[7,24] for details.

The shear strain rate due to phase transitions should not exceed the total deviatoric plastic strain rate, the latter of which includes the sum of contributions from slip, twinning, and phase transitions. Mathematically, this requirement leads to $2\dot{\epsilon}^P \geq \gamma^{\xi}\dot{\xi}$ and ensures that total flow never reduces local entropy. In notation of prior works,[7,25] $\dot{e}^P = \sqrt{\frac{2}{3}}\dot{\epsilon}^P$, where $\dot{\epsilon}^P$ is the magnitude of the deviatoric plastic deformation rate tensor. This magnitude is converted to the plastic strain rate $\dot{e}^P$ that is work conjugate to the von Mises stress via the factor of $\sqrt{\frac{2}{3}}$. An additional constraint on $\dot{\xi}$ is imposed to enforce this condition. The transformation shear is

defined as a function of local von Mises stress state $\bar{\sigma}^V$ as in earlier models of TRIP steels,[19,20] and it becomes zero if the total deviatoric plastic strain rate is zero:

$$\dot{\xi} = \begin{cases} \min(\dot{\xi}^t, 2\dot{\epsilon}^P/\gamma^\xi), \\ \dot{\xi}^t \qquad \text{if } \gamma^\xi = 0; \end{cases} \qquad \gamma^\xi = \begin{cases} \gamma_0^\xi \cdot \min(1, \bar{\sigma}^V/\sigma_0^{(0)}), \\ 0 \qquad \text{if } \dot{\epsilon}^P = 0; \end{cases} \quad \gamma_0^\xi \geq 0. \tag{9}$$

The transformation shear strain for local stress exceeding the datum yield stress is the material constant γ_0^ξ. The datum yield stress of the parent phase is $\sigma_0^{(0)} \geq 0$. Since $\dot{\epsilon}^P \geq 0$ and $\gamma^\xi \geq 0$ by definition, the first of Eq. 9 only restricts forward transformations (i.e., those with $\dot{\xi}^t > 0$). If $\gamma_0^\xi = 0$ (i.e., null transformation shear[5,22]), this constraint vanishes. Equation 1 is obeyed unconditionally by Eqs. 2–9.

Dependence of deviatoric strength on external magnetic field is implemented as follows in the composite flow model[7] for dual-phase ferromagnetic polycrystals. For each phase α, slip and twinning resistances are embedded in strength function $K^{\chi(\alpha)}$, whereas transition flow resistance is embedded in $K^{\xi(\alpha)}$. Since slip, twinning, and phase transformations may operate in parallel,[21,44]

$$1/K^{P(\alpha)} = 1/K^{\chi(\alpha)} + 1/K^{\xi(\alpha)}. \tag{10}$$

A smooth double-well function of ξ is used to modulate $K^{\xi(\alpha)}$, with zeroes at $\xi - \xi_0 = 0, 1$:

$$z^{\xi(\alpha)}(\xi; \theta, \boldsymbol{H}) = 4\iota^{(\alpha)}(\theta, \boldsymbol{H}) \cdot (\xi - \xi_0)(1 - \{\xi - \xi_0\}); \tag{11}$$

$$K^{\xi(\alpha)} = K^{\chi(\alpha)} \left(1/z^{\xi(\alpha)} - 1\right) \quad \Rightarrow \quad K^{P(\alpha)} = K^{\chi(\alpha)} \left(1 - z^{\xi(\alpha)}\right). \tag{12}$$

Values of $\iota^{(0,1)}$, which affect composite strength only for $\xi \neq \xi_0$ and hence depict phase interactions, can most generally depend on the local temperature and magnetic field.[7] However, the present software implementation[25] omits temperature dependence of $\iota^{(\alpha)}$ and sets ι the same for each phase $\alpha = 0, 1$. Linear dependence on the local field magnitude is prescribed analogously to Eq. 7:

$$\iota(|\boldsymbol{H}|) = \iota^{(0)}(|\boldsymbol{H}|) = \iota^{(1)}(|\boldsymbol{H}|) = \iota_0 + \iota_1 \mu_0 |\boldsymbol{H}|, \tag{13}$$

where ι_0 and ι_1 are constants.

The scalar function in Eq. 13 has range $\iota^{(\alpha)} \in (0, 1]$ when transformation strain accommodation induces softening in phase α. This permits prediction of sigmoidal

stress-strain curves witnessed in some TRIP steels.[19,20] For no such accommodation, $\iota^{(\alpha)} = 0$, and composite strength does not depend on magnetic field.

The second well in Eq. 11 is never attained in practice if $\xi_0 > 0$; in that case, some accommodation is permanent when $\xi \rightarrow 1$. The form in Eq. 11 is intended for situations when $\xi \geq \xi_0$ as in Clayton and Lloyd.[21] Conditional modifications are necessary to account for scenarios in which reverse transformation renders $\xi < \xi_0$.

An augmentation of the composite flow stress model for dual-phase polycrystal plasticity was introduced by Clayton and Lloyd[21] to allow for increased strength at very high rates of loading.[45–47] This strength increase is often attributed to increased viscous and phonon drag of dislocations. This augmentation was not used in two recent works[7,24] but is available in the present software implementation[25]:

$$K^{\chi(\alpha)} = k^{(\alpha)} \cdot \left(\dot{e}^P/\dot{e}_0\right)^{m^{(\alpha)}} \langle 1 - \bar{\theta}^{p^{(\alpha)}} \rangle [1 + k_s \langle \ln(\dot{e}^P/\dot{e}_s) \rangle]. \tag{14}$$

The additional material constants for shock dynamics are k_s and $\dot{e}_s > 0$, where the latter is generally a large strain rate for metals (e.g., on the order of 10^4/s). When $k_s > 0$, increased strength occurs for $\dot{e}^P > \dot{e}_s$. The other material constants entering Eq. 14 are defined in the past publications.[21,25]

2.2 Velocity Gradient Decomposition

The deformation gradient $\boldsymbol{F}$ follows the classical multiplicative split[48]:

$$\boldsymbol{F} = \nabla_0 \boldsymbol{x} = \boldsymbol{F}^E \boldsymbol{F}^P. \tag{15}$$

The thermoelastic deformation, which encompasses rigid-body rotation, is $\boldsymbol{F}^E$. The total inelastic deformation is $\boldsymbol{F}^P$, encompassing possible contributions from dislocation slip, deformation twinning, phase transformations, and damage mechanisms. Neither $\boldsymbol{F}^E$ nor $\boldsymbol{F}^P$ is generally integrable.[49] The total Eulerian velocity gradient $\boldsymbol{l} = \dot{\boldsymbol{F}}\boldsymbol{F}^{-1}$ is split into an elastic part $\boldsymbol{l}^E = \dot{\boldsymbol{F}}^E(\boldsymbol{F}^E)^{-1}$ and a plastic part $\boldsymbol{l}^P = \boldsymbol{F}^E\dot{\boldsymbol{F}}^P(\boldsymbol{F}^P)^{-1}(\boldsymbol{F}^E)^{-1}$. The spin tensor $\boldsymbol{\omega}$ (i.e., skew part of $\boldsymbol{l}$) and the deformation rate tensor $\boldsymbol{d}$ (i.e, symmetric part of $\boldsymbol{l}$) are additively decomposed into elastic $(\cdot)^E$ and plastic $(\cdot)^P$ parts.

For an isotropic polycrystal that remains isotropic throughout its deformation history, no preferred crystallographic texture should emerge. In the context of crystal

plasticity,[48,50–52] this implies that for every slip system-slip plane dyad $\boldsymbol{a}^{(i)} \otimes \boldsymbol{b}^{(i)}$, a complementary dyad of the form $\boldsymbol{b}^{(i)} \otimes \boldsymbol{a}^{(i)}$ is activated with equal probability. As such, the plastic spin averaged over the ensemble of active single crystal slip systems within an isotropic polycrystalline element should vanish, leading to $\boldsymbol{\omega}^P = \boldsymbol{0}$, and thus the total continuum spin is the elastic spin: $\boldsymbol{\omega} = \boldsymbol{\omega}^E$. Therefore,

$$\boldsymbol{l} = \boldsymbol{d}^E + \boldsymbol{d}^P + \boldsymbol{\omega}; \quad \boldsymbol{d}^E = (\boldsymbol{d}^E)^{\mathrm{T}}, \quad \boldsymbol{d}^P = (\boldsymbol{d}^P)^{\mathrm{T}}, \quad \boldsymbol{\omega} = -\boldsymbol{\omega}^{\mathrm{T}} = \boldsymbol{\omega}^E. \tag{16}$$

These kinematic assumptions, along with small deviatoric elastic stretch and small deviatoric elastic stretch rate, permit derivation[7,21] of the objective Jaumann rate equation for the deviatoric spatial lattice stress (i.e., contribution of elastic shear strain to Cauchy stress). This equation is conveniently integrated in time to update the deviatoric Cauchy stress using a radial return method, as discussed by Clayton et al.[7] These assumptions are standard in the finite plasticity and computational plasticity literature.[53–55] The total Cauchy stress is found from the thermoelastic volume change $\ln J^E = \mathrm{tr}\boldsymbol{e}^E$ and temperature, both of which affect the lattice pressure, the deviatoric spatial lattice stress, the phase and damage fractions ξ and ϕ, and the spatial magnetic field variables $\boldsymbol{B}$ and $\boldsymbol{M}$. None of the kinetic laws or the temperature rate equation require $\boldsymbol{F}^E$ or $\boldsymbol{F}^P$ explicitly; rather, only the elastic and plastic deformation rates are used. There is no need for calculation of any of $\boldsymbol{R}^E$, $\boldsymbol{U}^E$, $\boldsymbol{R}^P$, or $\boldsymbol{U}^P$ from polar decompositions, for example, motivated by the Cayley-Hamilton theorem.[56] Costly matrix inversions are also avoided.

However, the present system of equations can be expanded to explicitly calculate these quantities at increased computational expense. Given $\boldsymbol{F}$, $\boldsymbol{l}$, and the total inelastic deformation rate $\boldsymbol{d}^P$ from the kinetic equations[7,25] for plastic flow, phase transitions, and damage, the elastic velocity gradient is found as $\boldsymbol{l}^E = \boldsymbol{l} - \boldsymbol{d}^P$. The elastic deformation can then be found from time integration of the differential equation $\dot{\boldsymbol{F}}^E(t) = \boldsymbol{l}^E(t)\boldsymbol{F}^E(t)$. Next, $\boldsymbol{F}^P$ can be calculated from $\boldsymbol{F}^P(t) = (\boldsymbol{F}^E)^{-1}(t)\boldsymbol{F}(t)$, where matrix inversion is needed. Finally, rotations and stretches of $\boldsymbol{F}^E$ and $\boldsymbol{F}^P$ could be obtained from calculating their polar decompositions.[56]

For simple problems, elastic and plastic rotation tensors can be deduced directly. For example, if a sample is deformed in uniaxial tension then rotated rigidly, all rotation will be embedded in $\boldsymbol{R}^E$ since $\boldsymbol{d}^P = \boldsymbol{0}$ during rigid body rotation. On the other hand, if the sample is rotated rigidly while undergoing plastic deformation $\boldsymbol{d}^P \neq \boldsymbol{0}$,

neither $\boldsymbol{R}^E$ nor $\boldsymbol{R}^P$ can be discerned intuitively a priori, but rather each would need to be calculated using the preceding procedure if sought for curiosity (recall, the distinct elastic and plastic rotation angles are not required by the isotropic constitutive model). Symmetry of $\boldsymbol{l}^P$ does not require that $\boldsymbol{F}^P$ be symmetric.

An alternative formulation can be envisioned whereby a kinetic law for $\dot{\boldsymbol{U}}^P$ (e.g., the rate of one possible Lagrangian plastic metric implemented by Miehe[57]) is prescribed, in conjunction with the constraint that plastic rotation $\boldsymbol{R}^P = \boldsymbol{1}$ for polycrystals. In this case, $\boldsymbol{F} = \boldsymbol{R}\boldsymbol{U} = \boldsymbol{R}^E\boldsymbol{U}^E\boldsymbol{U}^P$ would emerge, and $\boldsymbol{R}^E = \boldsymbol{R}$ such that total rotation is always elastic. Another similar approach would prescribe a kinetic law for the symmetric part of $\dot{\boldsymbol{F}}^P(\boldsymbol{F}^P)^{-1}$, reasonably assuming that the skew part of $\dot{\boldsymbol{F}}^P(\boldsymbol{F}^P)^{-1}$ vanishes identically for plastic isotropy. This approach, advocated in past work by the author,[24] has the apparent physical advantage that the true plastic spin, rather than its elastic push-forward, vanishes. However, since $\boldsymbol{F}^E$ is non-singular, vanishing of the true plastic spin leads to vanishing of $\boldsymbol{\omega}^P$. Both alternatives[24,57] are perhaps more physically justified than the current prescription[7,25] in which the kinetically prescribed flow rate $\boldsymbol{d}^P$ contains intrinsic elastic push-forward terms, though effects of the stretch contributions of these terms should be small for ductile metals. However, these quoted alternatives would require sophisticated,[58] and likely costly, numerical implementations for updating the stress and other constitutive variables (e.g., the Jaumann rate derived previously[7,25] would not necessarily apply). On the other hand, the assumptions and approximations used in the current framework take advantage of existing, efficient numerical algorithms for explicit dynamic finite element (FE) computations,[21,42,53,54,59] thus justifying their use.

2.3 Remarks on Kinetics and Dissipation

The kinetic laws prescribed by Clayton et al.[7,25] for phase transitions, damage, and plastic flow are physically justified based on experimental evidence and are fully consistent with the laws of thermodynamics, namely, non-negative dissipation is ensured for each mechanism ultimately affecting the Clausius-Duhem inequality. However, in each case, no linear relationship between conjugate thermodynamic force and kinetic rate is imposed, nor is any dissipation potential used. However, such a potential exists in the theory[7] for the deviatoric part of the total plastic flow rate when energy storage from dislocations (i.e., stored energy of cold work) is omitted.

For phase transitions, a linear relaxation kinetic law to a metastable state surface is used, which has been proven reasonably successful for reproducing experimentally observed phase change kinetics for Fe and other ferrous alloys.[5,22,24] The conjugate thermodynamic driving force to the phase fraction ξ is the Gibbs free energy difference $-\Delta^*\mathbb{G}$, which affects the metastable surface in a nonlinear way. Dissipation from transitions is always non-negative according to this theory, elaborated in Section 2.1.

For evolution of porosity ϕ, a direct evolution law for the void volume fraction is prescribed following Cocks and Ashby,[60,61] which in turn always leads to non-negative dissipation since the model's elastic coefficients can only degrade with increasing damage. The net conjugate thermodynamic force is $\hat{\Xi}$. This force does not explicitly enter the kinetic law, but the tensile pressure, which is part of $\hat{\Xi}$, is a primary factor controlling the growth of porosity. A similar Cocks-Ashby model[62] has been successfully used elsewhere to represent ductile failure of steels.[21,53]

For plastic flow, an associative flow rule with normality and Kuhn-Tucker conditions[54] is imposed for the deviatoric part $\bar{\boldsymbol{d}}^P$. A Taylor-Quinney factor $\hat{\beta}$ locally averaged over constant values for each phase is used. So long as $\hat{\beta} \geq 0$, net plastic dissipation from plastic flow less energy storage from cold work[63] is always non-negative, and the theory is thermodynamically consistent. However, unless $\hat{\beta} = 1$, deviatoric plastic flow does not maximize net dissipation, since some fraction of plastic working increases the free energy (i.e., χ is not fully dissipative[7,21,24,64]). Though alternative formulations exist for various steels,[19,20,65] similar kinetic frameworks have been successfully used elsewhere for capturing experimental data on ferrous alloys undergoing slip, twinning, and phase transitions.[21,37,66] The total plastic strain rate $\boldsymbol{d}^P$, consisting of deviatoric flow and volume changes from phase transitions and voids, is not strictly required to satisfy any normality conditions or to be derivable from any dissipation potential.[62]

Now-classical and customary concepts[67] have been proposed for constructing kinetic laws that unconditionally produce non-negative dissipation (i.e., lead to non-negative entropy production from state variables). Perhaps the simplest physically justified proposition, attributed to Onsager,[68] is a linear relationship between thermodynamic fluxes (i.e., kinetic rates) and their conjugate thermodynamic forces. The Onsager method was generalized by Ziegler[69] to allow for nonlinear force-flux

relations via dissipation potentials whose derivatives with respect to thermodynamic forces produce the corresponding fluxes. Accordingly, the local material state tends to evolve toward one of minimum free energy, though exceptions exist.[70]

Elsewhere, models incorporating principles of Onsager and Ziegler have been implemented for phase transitions and plastic flow. For example, in a model for Fe,[43] a kinetic law for the phase transition rate linearly proportional to $-\Delta^*\mathbb{G}/\theta$, consistent with Onsager's theory for isothermal conditions, was used for shock loading. In work of Miehe,[57] kinetic laws were derived for plastic flow and hardening variables using a shared convex potential consistent with Ziegler's approach and maximum dissipation. While the present model framework does not obey all such principles—which are always sufficient but are not always necessary for thermodynamic admissibility—it is consistent with non-negative net dissipation and produces sound agreement with experimental observations, thus providing its justification.

2.4 Physical Processes at Different Time Scales

The general theoretical-numerical framework[7,25] simultaneously resolves mechanical, thermal, and electromagnetic phenomena. Each of these three classes of phenomena acquires a characteristic time from its corresponding governing equation(s). The balance of linear momentum furnishes the time t_{mech} for mechanical signals (i.e., stress waves). To first order, the longitudinal sound velocity $c_L = [(\mathsf{B}_0 + \frac{4}{3}\mathsf{G}_0)/\rho_0]^{1/2}$ produces the characteristic time $t_{\text{mech}} \approx L/c_L$, where L is a representative length over which the signal propagates. The balance of energy in conjunction with the assumption of constant isotropic thermal conductivity κ produces the characteristic time for thermal diffusion $t_{\text{therm}} \approx L^2 c^V/\kappa$.

Derivation of the characteristic time for electromagnetic phenomena follows from Maxwell's equations of quasi-magnetostatics in conjunction with the assumption of constant isotropic electrical conductivity Σ. The quasi-magnetostatic approximation[24,29] is invoked in Ampere's law, whereby $|\epsilon_0 \partial_t \boldsymbol{E}| \ll |(\nabla \times \boldsymbol{H}) - \boldsymbol{J}|$ for finite $\boldsymbol{H}$ and/or finite $\boldsymbol{J}$. Conditions for confidence of the quasi-magnetostatic approximation are discussed by Landau et al.[71]: frequencies $\hat{\omega}$ of applied magnetic field, electric field, and current must be small versus speed of light in vacuum divided by characteristic length: $\hat{\omega} \ll \mathsf{c}/L$. Accordingly, magnitudes of time rates of electric field (and thus electric current if proportional) must remain small in a relative sense. In this approximation, electromagnetic waves can be interpreted to propagate with

infinite velocities in free space, and electric current signals are effectively instantaneous in conductors. The quasi-static forms of Maxwell's equations do not enable resolution of optical phenomena, for example propagation of light that occurs at a very fast time scale impossible to resolve simultaneously in FE discretizations fully resolving acoustic and thermal transients.

Taking the curl of Ampere's law, substituting for the electric current from Ohm's law, and applying Faraday's law gives a diffusion-like equation for magnetic field $\boldsymbol{H}$, generalizing that of Landau et al.[71] to Galilean-invariant form[24]:

$$\begin{aligned} \nabla \times \nabla \times \boldsymbol{H} = \nabla \times \mathsf{J} = \Sigma \nabla \times \mathsf{E} = -\Sigma \overset{*}{\boldsymbol{B}} \\ \Rightarrow \quad \overset{*}{\boldsymbol{H}} = \{\mu_0 \Sigma\}^{-1} [\nabla^2 \boldsymbol{H} - \nabla(\nabla \cdot \boldsymbol{M})] - \overset{*}{\boldsymbol{M}}. \end{aligned} \tag{17}$$

Given the magnetic permeability μ, the time for magnetic diffusion from Eq. 17 is derived as $t_{\text{mag}} \approx \Sigma \mu L^2$.[24,71]

In simulations, L corresponds to the minimum size of elements of the grid or mesh, and the time step size Δt should be smaller than the minimum characteristic time for accuracy and stability (i.e., the Courant-Friedrichs-Lewy condition) if explicit integration methods are used, as is conventional for the momentum balance.[41,42,59] As an example, take $L = 1$ mm and invoke physical properties of Fe,[24] with $\mu = \mu_0$ the limiting case for magnetic diffusion. The longitudinal sound speed is $c_L \approx 6$ km/s, giving $t_{\text{mech}} \approx 0.17\,\mu$s. Thermal diffusivity $\kappa / c^V \approx 22$ mm^2/s of iron produces $t_{\text{therm}} \approx 45$ ms. The electrical conductivity $\Sigma = 10^7$ A/V·m produces $t_{\text{mag}} \approx 13\,\mu$s. Thus, the limiting case is $\Delta t < t_{\text{mech}}$, meaning that sound speed here controls the minimum global time step. For most crystalline solids of current interest, $t_{\text{mech}} \ll t_{\text{therm}}$. However, if electrical conductivity Σ is very low, then t_{mag} can be prohibitively small. For this reason, implicit integration methods are commonly used in magnetohydrodynamics host codes[41,42] for stable solution of the magnetic diffusion equation with larger step sizes.

Step Δt should also be small enough to resolve local kinetic processes, namely viscoplasticity, phase transitions, and damage. For each time increment, changes in e^P, ξ, and ϕ should not be severe, as suitably regulated by algorithms for modeling of each mechanism.[7,25]

3. Simulation Protocols

3.1 Material and Parameters

The composition in weight (wt.) % is as follows for the ferrous AR alloy of present study[7] designed and fabricated by ARL: C 0.17, Mn 8.75, Si 0.68, Cr 12.01, Ni 2.5, N 0.07, and Fe 75.82. The material initially consists of three phases: γ (FCC), ϵ (HCP), and α (BCC). Before deformation, volume fractions for the AR alloy are γ of 0.806, ϵ of 0.136, and α of 0.058.

The model tracks fractions of only two phases simultaneously, one with volume fraction $\xi^{(0)} = 1 - \xi$ corresponding to the parent phase, the other with fraction $\xi^{(1)} = \xi$ corresponding to the child phase. Forward transformation entails an increase in ξ. For the present materials, the close-packed phases γ and ϵ are combined into a single γ/ϵ phase, with the remaining α phase corresponding to the parent phase. Properties that depend on phase volume fractions of γ and ϵ phases are obtained for the composite close-packed phase via a mixture rule[7] with the initial volume fractions of γ and ϵ phases. Labeling the compressive (i.e., densifying) transformation $\alpha \rightarrow \gamma/\epsilon$ as the forward transformation, $\xi_0 = \xi(t = 0) = 0.942$ is the initial volume fraction of the dense child phase. For complete transformation from the BCC to the FCC and HCP phases, $\xi : 0.942 \rightarrow 1$. Notably, only a small fraction of the material (0.058) is locally available for this pressure-induced transition.

With the exceptions of the magnetic field-affected kinetic parameters α_0^F, α_1^F, β_0^F and β_1^F in Eq. 7 and ι_0 and ι_1 in Eq. 13, all material parameters for the AR alloy are taken verbatim from the recent work of Clayton et al.[7] The complete list is lengthy and omitted here for brevity. Regarding parameters of Eq. 7, only those for forward transitions are required for the present study when the forward transformation is defined as $\alpha \rightarrow \gamma/\epsilon$. Values of α_0^F, α_1^F, β_0^F, β_1^F, ι_0, and ι_1 considered in forthcoming simulations are listed in Table 1. Parameters have not been calibrated for the $\alpha \rightarrow \gamma/\epsilon$ transition for the AR alloy in prior work. Herein, Model 1 applies the kinetic parameters for the isothermal $\gamma/\epsilon \rightarrow \alpha$ transformation of the same AR alloy as calibrated to quasi-static tensile experiments.[7] With the exception of dimensionless parameter ι_0 that is held fixed, Model 2 applies the kinetic parameters for the $\alpha \rightarrow \epsilon$ transition in pure Fe as calibrated to shock compression experiments.[3,7]

Table 1 Kinetic parameters for magnetic field effects on phase changes and inelasticity

Parameter (units)	Model 1	Model 2
α_0^F (MPa)	469	0
α_1^F (MPa/T)	7.78	-36.0
β_0^F (MPa)	22.0	90.5
β_1^F (MPa/T)	7.78	0.0
ι_0 (-)	0.195	0.195
ι_1 (1/T)	-0.062	0.0

The relaxation time for transition kinetics $\tau^R = \tau^F = 25\,\text{ns}$ is assumed identical to that of pure Fe.[7,24] Equation 14 is implemented for dynamic calculations with $k_s = 0.25$ and $\dot{e}^P = 10^4$/s, as used for a different austenitic TRIP steel in past research.[21] The strain-rate and temperature sensitivity of the flow stress entering Eq. 14 and the Taylor-Quinney factor $\hat{\beta}$ have not been measured for this alloy. Therefore, values of those of a different TRIP steel[21] are used out of necessity, assumed the same for both phases $\alpha = 0, 1$: $m^{(\alpha)} = 0.003$, $p^{(\alpha)} = 0.6$, $\hat{\beta}^{(\alpha)} = 0.8$, with $\dot{e}_0 = 10^{-3}$/s.

3.2 Loading Conditions

Calculations in prior work[7] considered loading applied so slowly that conditions were mechanically quasi-static, not exceeding moderate pressures (e.g., $p < 60$ GPa). These conditions sought to replicate hydrostatic compression, metastable Hugoniot states, and low-rate tensile experiments. In each case, the complete dynamic theory, as well as dynamic numerical procedures, remained valid and was applied. However, the numerically imposed strain rates were low enough such that, in each loading increment, transformation followed the metastable equilibrium path (i.e., $\xi(t) \to \xi^m(t)$), the influence of strain rate on flow strength was negligible, and any damage growth was unaffected by the time scale since the damage rate is proportional to the flow rate.[7,21,25]

In this report, new problems evaluate the model's performance at much higher pressures and loading rates. New calculations herein only consider the AR ferrous alloy. Experimental data for this alloy are not available at the extreme loading conditions simulated here, so comparisons are made with data on Fe[6,72] and other steels.[73]

A material element within a cylinder of the alloy is modeled. For metastable equilibrium,[5] slow loading conditions are applied to mimic those trailing a planar shock wave moving in direction $\boldsymbol{i}$ along the length of the cylinder, wherein quasi-static approximations hold. Within the rise of a structured shock wave, all quasi-static conditions need not apply. However, the quasi-magnetostatic approximation[71] is still thought to be reasonable within transformation shock waves of strength considered here. For an applied strain rate on the order of 10^6/s and a compressive strain of 0.1 achieved within the transformation wave, the characteristic rise time is 100 ns. This is orders of magnitude larger than the characteristic time for propagation of electromagnetic waves over a domain size of 1 cm (i.e., around 0.03 ns). For a steady transformation wave speed of 5 km/s, the shock width in this thought experiment would be 500 μm.

Uniaxial strain compression is applied in the 1-direction denoted by unit vector $\boldsymbol{i}$, at a constant rate:

$$\boldsymbol{F}(t) = \mathbf{1} - \hat{\epsilon}(t)\boldsymbol{i}\otimes\boldsymbol{i}, \qquad \hat{\epsilon}(t) = \dot{\hat{\epsilon}}\,t = 1 - J(t) = 1 - \rho_0/\rho(t) \geq 0. \tag{18}$$

Two rates are considered: $\dot{\hat{\epsilon}} = 10^{-3}$/s and $\dot{\hat{\epsilon}} = 10^{6}$/s, where the former (static) is representative of metastable Hugoniot states in regions behind a shock wave that has passed. The latter (dynamic) is representative of rapid straining within a shock front.[74–76] Compressions up to 35% achieve extreme pressures. Insulated and adiabatic thermal conditions are imposed with a starting temperature of $300\,\mathrm{K}$.

In some calculations, an external magnetic field $\boldsymbol{H}$ of strength $\mu_0 H^\infty = 2\,\mathrm{T}$ is applied parallel to the compression direction. Across a shock, normal continuity of the magnetic flux density $\boldsymbol{B} = B\boldsymbol{i}$ implies the signed magnitude $B =$ constant within the cylindrical specimen during the compression process, as required by Maxwell's equations.[24,29] Magnetic loading conditions for this field orientation, denoted as "parallel," are imposed as

$$B = \begin{cases} \mu_0 H^\infty & (H^\infty \ll H^S), \\ \mu_0(H^\infty + M_0^S) & (H^\infty \gtrsim H^S). \end{cases} \tag{19}$$

Here, $H^S = 0.05$ T is the threshold for magnetization in the ferroelectric phase of the polycrystal, assigned a magnitude applicable to pure Fe.[24] The initial saturation magnetization of the composite, consisting of a low fraction of ferromagnetic α

phase, is calculated a priori from thermodynamic parameters[7] of the initial phases as $\mu_0 M_0^S = 0.09537$ T.

In other forthcoming calculations, a constant magnetic field of strength $\mu_0 H = 2\,\mathrm{T}$ is applied transverse to the direction of straining,[6] in the 2-direction denoted by $\boldsymbol{j}$: $\boldsymbol{H} = H\boldsymbol{j}$ with $\boldsymbol{i} \cdot \boldsymbol{j} = 0$. For a relatively short cylinder (e.g., a disc used as a target for plate impact), the assigned condition $H =$ constant in the sample of material is consistent with tangential continuity of field $\boldsymbol{H}$ across its flat faces as required by Maxwell's equations.[29] This applied field condition is denoted as "perpendicular."

The longitudinal Cauchy stress component P and a measure of shear stress τ are defined as follows from Cauchy stress $\boldsymbol{t}$, here equal to $\boldsymbol{\sigma}$ which is symmetric[7]:

$$P = -\boldsymbol{t} : (\boldsymbol{i} \otimes \boldsymbol{i}), \qquad \tau = P + \boldsymbol{t} : (\boldsymbol{j} \otimes \boldsymbol{j}). \tag{20}$$

For the present loading protocols, $P > 0$ and $\tau > 0$. In the absence of a magnetic field, $t_{22} = t_{33}$ and $|\tau|$ equals the von Mises stress $\bar{\sigma}^V$. Since the calculations invoke displacement control with spatially constant field variables $\boldsymbol{F}, \boldsymbol{H}, \boldsymbol{B}, \boldsymbol{M}, \boldsymbol{t}, \theta$, no spatial discretization (e.g., FE mesh) is required. Methods are akin to single integration-point calculations within one solid element, for example.

4. Numerical Results

4.1 Metastable States

Calculated results for adiabatic quasi-static loading at $\dot{\hat{\epsilon}} = 10^{-3}$/s are shown in Fig. 1. In these calculations, the external magnetic field, if nonzero (i.e., $\mu_0 H^\infty = 2$ T) is parallel to compression direction $\boldsymbol{i}$. Longitudinal stress P is reported versus density in Fig. 1, where curves of P are generally similar among both models and both magnetic field strengths. For Model 1, close inspection of numerical data underlying Fig. 1b reveals a slightly stiffer $P - \rho$ Hugoniot for a 2 T field than for null field. For example, at $\rho_0/\rho = 0.97$ according to Model 1, $P = 6.785$ GPa for $H = 0$ and $P = 6.817$ GPa for a 2 T field. Similarly, small differences in results for Model 2 for field strengths $\mu_0 H^\infty$ of 0 and 2 T also cannot be visually discerned in Fig. 1d. At $\rho_0/\rho = 0.97$ according to Model 2, $P = 6.656$ GPa for $H = 0$ and $P = 6.623$ GPa for a 2 T field.

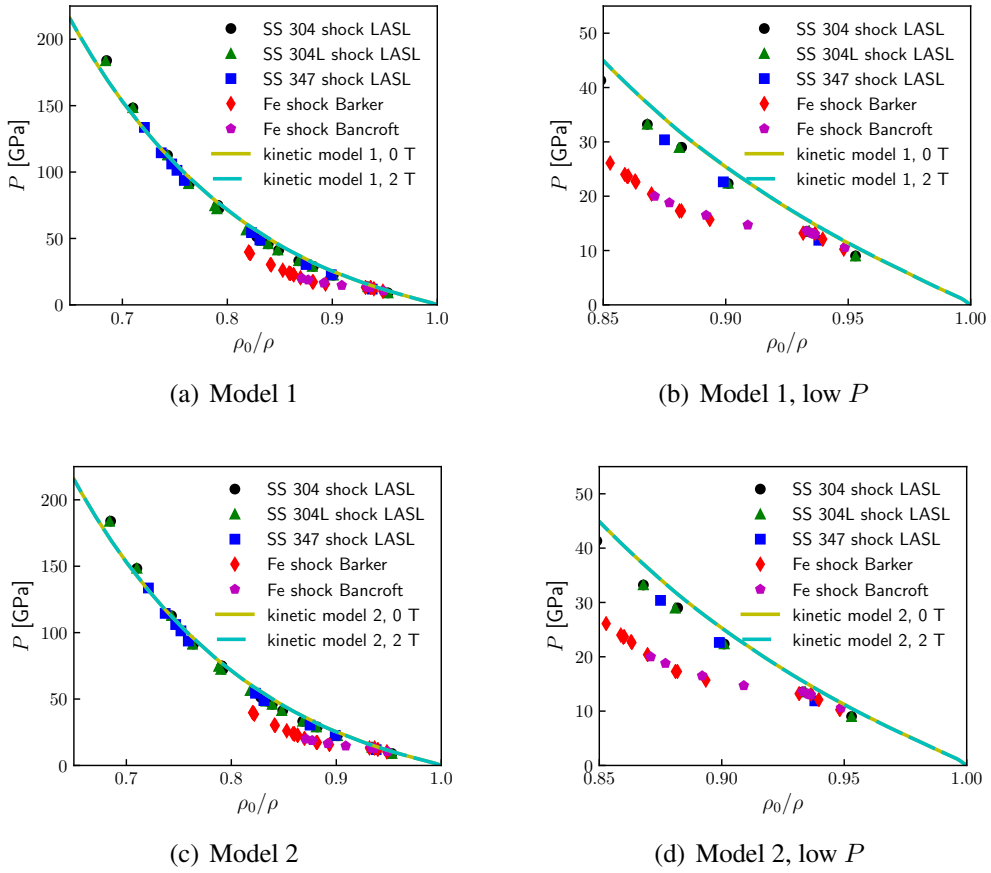

(a) Model 1

(b) Model 1, low P

(c) Model 2

(d) Model 2, low P

Fig. 1 Axial stress P for adiabatic uniaxial strain compression. Curves are metastable state predictions for AR alloy, with or without an external 2 T magnetic field parallel to the compression direction. Experimental Hugoniot data are for stainless steel[73] and pure Fe.[6,72] Results are as follows: (a) Model 1 and experiments, (b) Model 1 and experiments, lower P range, (c) Model 2 and experiments, and (d) Model 2 and experiments, lower P range.

As discussed in prior work,[7,25] the logarithmic equation of state[75,77] (EOS) is implemented in the Helmholtz free energy potential to relate lattice pressure, thermoelastic compression, and temperature. Predictions in Fig. 1 for the adiabatic metastable response are similar to experimental Hugoniot data of three kinds of stainless steel (SS): 304, 304L, and 347,[73] especially in the pressure range between 50 and 150 GPa. These similarities provide some confidence in the EOS and its implementation in the present framework. Even closer agreement at very high P exceeding 150 GPa could be achieved by including the contribution of shock dissipation to entropy production, of order three in $\hat{\epsilon}$ as derived analytically elsewhere.[77] This contribution is omitted in the present homogeneous-deformation calculations.

The AR alloy undergoes densification with an $\alpha \rightarrow \gamma/\epsilon$ phase transformation, but

since the initial α fraction is just under 6%, the effect on the average pressure (p or P) is gradual and relatively small. This in contrast to pure α-iron, which undergoes a complete (100%) transformation to the ϵ phase, leading to a more abrupt mass density increase and smaller value of P at the same ratio ρ_0/ρ as evident in the experimental data.[6,72] Predicted P versus ρ Hugoniot responses are affected very little by the choice of kinetic parameters for Model 1 versus Model 2 in Table 1. Comparing underlying data for Figs. 1b and 1d, a slightly higher P versus ρ curve for a 2 T field is observed when kinetic Model 1 is used rather than Model 2 because field-assisted transformation occurs at lower P and ρ in the latter. These differences exist in the calculated data, but they are too small to be visually discerned in Fig. 1.

Table 2 lists longitudinal stress P for initiation of the $\alpha \rightarrow \gamma/\epsilon$ transformation as predicted by the model for both parameter sets of Table 1. Results for both magnetic field orientations (i.e., parallel and perpendicular to $\boldsymbol{i}$) are reported. Also shown are model predictions[7] for the $\alpha \rightarrow \epsilon$ transformation in pure Fe.

Table 2 Predicted shock pressure P for initiation of $\alpha \rightarrow \gamma/\epsilon$ transition

Material	Model	External H Field (T)	Field direction	Pressure P (GPa)
AR alloy	1	0	...	6.196
	1	2	parallel	6.634
	1	2	perpendicular	6.631
AR alloy	2	0	...	4.494
	2	2	parallel	4.112
	2	2	perpendicular	4.112
Fe	...	0	...	13.187
	...	2	parallel	11.800
	...	2	perpendicular	11.712

The tabulated predictions for pure Fe[7] have been validated versus experimental data, with[3] and without[5,38] applied magnetic fields (i.e., "H fields"). Transition pressure is defined as the value of P for which $\dot{\xi}$ first exceeds zero as the composite mass density concurrently increases. The following trends are recognized in Table 2:

- The external H field increases the initiation pressure of the AR alloy by 6.6% for Model 1.
- The external H field decreases the initiation pressure of the AR alloy by 8.5%

for Model 2.

- The predicted initiation pressure of the AR alloy is 2.3 to 2.5 GPa higher for Model 1 than for Model 2.
- The orientation of the H field has little or no effect (e.g., much less than 1% difference) on initiation pressure for the AR alloy.
- The transition pressure of pure Fe is at least 7 GPa larger than that predicted for the AR alloy at null H.
- The effect on transition pressure of orientation of the H field is non-negligible but very small (e.g., around 1% difference) for pure Fe.

The significantly lower transition pressure of the AR alloy compared to pure Fe when Model 2 kinetic parameters are used is attributed to several factors. First, the thermodynamic properties of the alloy differ from those of pure Fe due to compositional (e.g., chemical and phase) differences. Second, the transformation shear strain $\gamma_0^\xi = 0.1$ is finite for the AR alloy ascertained from tensile test data and modeling,[7,19] but the vanishing of transformation shear strain, $\gamma_0^\xi = 0$, is assumed for pure Fe.[5,24,38] The shear driving force affecting $\Delta^*\hat{\mathbb{G}}$ in Eq. 8 is thus negative for the AR alloy under uniaxial compression, lowering the Gibbs energy barrier and promoting transformation via $\dot{\xi} > 0$. This driving force is omitted in the model for pure Fe.[5,24,38] Model 1 also yields a lower predicted transition pressure of the alloy relative to that of pure Fe, albeit not as low as Model 2.

4.2 Dynamic Compression

Calculated results for adiabatic dynamic loading at $\dot{\hat{\epsilon}} = 10^6$/s are shown in Fig. 2. In these calculations, the external magnetic field, if nonzero (i.e., $\mu_0 H^\infty = 2$ T) is parallel to compression direction $\boldsymbol{i}$. On the abscissa, uniaxial strain is measured by ρ_0/ρ, the density ratio of the composite, equal to the inverse of the specific volume ratio. Transformation volume fraction ξ in Fig. 2a increases with increasing ρ but is scantly affected by the external magnetic field. Transformation commences at a lower density for Model 2 than for Model 1. Trends are consistent with the quasi-static results in Table 2.

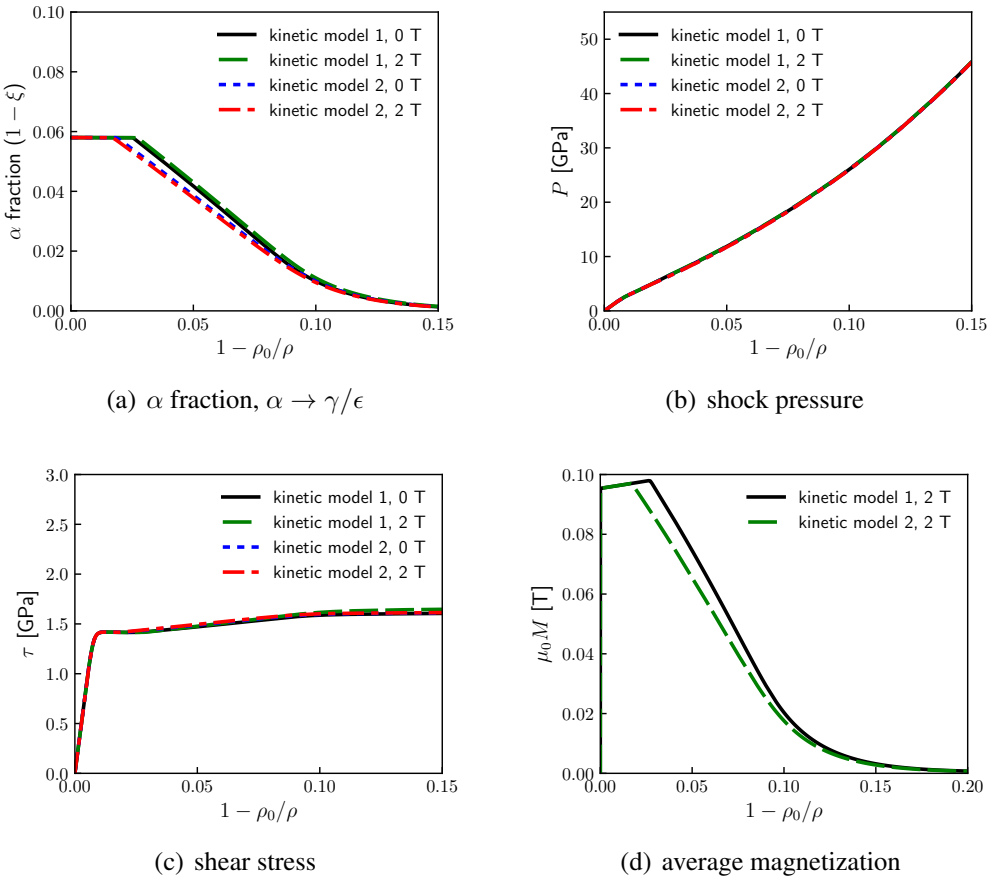

(a) α fraction, $\alpha \to \gamma/\epsilon$

(b) shock pressure

(c) shear stress

(d) average magnetization

Fig. 2 Dynamic adiabatic uniaxial strain compression at strain rate $\dot{\hat{\epsilon}} = 10^6$/s; AR alloy, model predictions vs. mass density ratio ρ/ρ_0 with or without external 2 T magnetic field parallel to compression direction: (a) fraction of BCC α phase $1 - \xi$, (b) longitudinal stress (i.e., shock pressure P), (c) shear stress, and (d) average spatial magnetization (vanishes for 0 T external field)

Though difficult to resolve in Fig. 2a, a nonzero magnetic field H impedes the phase transition for Model 1, similar to observations in prior work[7,25] for the reverse transformation in this alloy. Here, both the magnetostatic energy difference and the transition kinetic barriers tend to inhibit transformation from ferromagnetic to paramagnetic phases as H increases. For example, at the lower loading rate pertinent to Table 2, the transition shock pressure increases from 6.196 to 6.634 GPa as the H-field increases from 0 to 2 T. At the present higher loading rate of 10^6/s, the transition start pressure increases similarly from 6.234 to 6.636 GPa. This behavior is physically expected given the prescribed yet experimentally uncertain parameters, lending some confidence to the implementation[25] of the phase change model.

Differences in shock stress P exist, similar to the quasi-static case, but these cannot be discerned among the two models and two field strengths (0 versus 2 T) in Fig. 2b. Differences in shear stress τ of Eq. 20 are detectable between predictions of different Models 1 and 2 in Fig. 2c, but these differences are relatively small, no more than around 50 MPa or 3% of τ. The model predicts an approximate doubling of strength from static to highly dynamic conditions due to rate sensitivity and dislocation drag effects included in Eq. 14. Effects of H on τ are small, yet visible, at compressions exceeding 10%. The high-pressure strength profiles in Fig. 2c are comparable to those for several other primarily austenitic steels,[21] providing some confidence in the current viscoplasticity implementation.

Magnetization per unit spatial volume $M = \xi M^{(1)} + (1-\xi) M^{(0)}$ is shown in Fig. 2d, with $M^{(1)}$ the magnetization of the close-packed paramagnetic phase(s) of volume fraction $\xi^{(1)} = \xi$ and and $M^{(0)}$ the magnetization of the BCC ferromagnetic phase of fraction $\xi^{(0)} = 1 - \xi$. Since the magnetization of the paramagnetic γ/ϵ phase is nearly negligible (0.0004 T) for $\mu_0 H^\infty = 2$ T, the average magnetization M consists nearly entirely of the contribution of the α phase. Prior to initiation of transformation, M increases slightly with increasing ρ since spatial volume per unit mass decreases with increasing density while the magnetization per unit mass is constant. As transformation proceeds, $\xi \rightarrow 1$ and the fraction of the ferromagnetic BCC α phase goes to zero, leading to negligible M at large compression $\rho/\rho_0 \geq 1.25$. Results are logical given the transformation profiles in Fig. 2a: as the ferromagnetic α phase transforms into the weakly paramagnetic close-packed phases, magnetization drops drastically. Magnetization M is defined as zero for $\mu_0 H^\infty < H^S = 0.05$ T per Eq. 19. In the absence of an aligning field, magnetic spins are assumed randomly oriented in the polycrystal so net magnetization vanishes.[24,29]

The predicted volume fraction of the less dense α phase is compared at low and high loading rates versus longitudinal stress (i.e., shock pressure P) in Fig. 3. At the dynamic rate of loading in Fig. 3b, transformation to the denser close-packed phases proceeds more gradually with increasing P than for quasi-static loading in Fig. 3a. The loading duration for the former is on the order of 100 ns, only around four times the phase transition relaxation time $\tau^F = \tau^R = 25$ ns. The dynamic phase transition lags the applied compression due to the finite time scale of transformation kinetics, and it does not fully complete ($\xi \rightarrow 1$) until around 60 GPa. This phenomenon would produce spreading of plastic transformation wave under shock loading.[5,22,38]

In contrast, at the lower rate of loading, the transition is nearly linear versus P and completes by around 30 GPa.

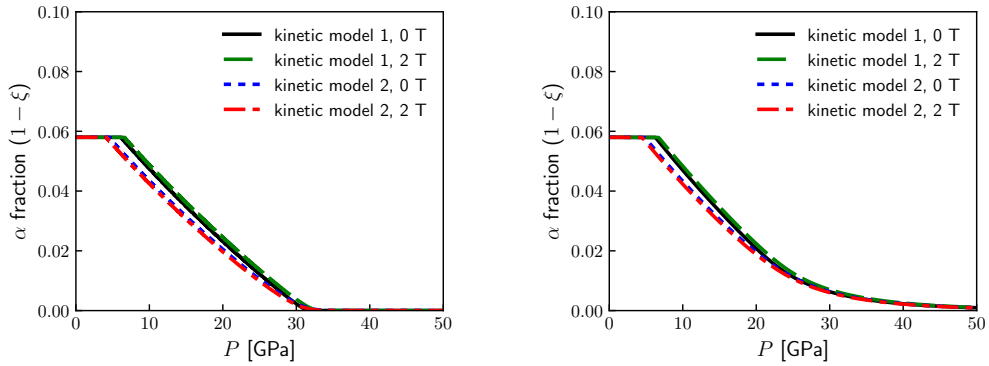

(a) quasi-static (b) dynamic

Fig. 3 Predicted fraction of BCC phase $1-\xi$ vs. shock pressure P: (a) quasi-static compression $\dot{\hat{\epsilon}} = 10^{-3}$/s and (b) dynamic compression $\dot{\hat{\epsilon}} = 10^{6}$/s

5. Conclusions

Material point simulations have modeled dynamic adiabatic compression of a ferrous alloy immersed in an external magnetic field. A continuum multiphysics constitutive model, developed and advanced in recent prior works by the author and collaborators, has been used in these simulations. Different conceivable parameter sets, not directly acquirable from scarce existing data, that dictate magnetic field-dependent kinetics for $\alpha \leftrightarrow \gamma/\epsilon$ phase transformations have been investigated. Boundary conditions approximate those experienced by an element of material subjected to planar shock compression witnessed in recent experiments at ARL.

Predicted Hugoniot stress-volume responses show very little effect of magnetic field, regardless of transition parameters. The Hugoniot responses of the model reasonably agree with experimental data on three stainless steels, providing confidence in the logarithmic pressure-volume-temperature EOS for shock pressures up to 150 GPa. The predicted dynamic shear strength of the alloy is also similar to that of other austenitic steels. Magnetization is affected by both the choice of transition kinetic parameters and the magnitude of the external field.

With or without an applied field, the present ferrous alloy is predicted to initiate transition to its denser phases at pressures less than around half of those for pure

Fe. Transformation initiation pressures are predicted to vary up to on the order of 10% for a 2 T field. Parameters obtained from isothermal static extension of the alloy lead to an increase in initiation pressure with increasing field strength. Parameters borrowed from a model of shock compression of pure Fe lead to a decrease in transition initiation pressure with increasing external field strength. Predicted differences in constitutive responses for magnetic fields aligned parallel or perpendicular to the compression direction are nearly negligible.

The current model predictions await confirmation from dynamic experimental data. Such data should also enable refinements of kinetic parameters as well as other continuum model features for this class of alloys in the adiabatic high-strain rate, high-pressure regime. Calculations and comparisons with experiments for the HT alloy are also planned.

6. References

1. Joo H, Kim S, Koo Y, Shin N, Choi J. An effect of a strong magnetic field on the phase transformation in plain carbon steels. Metallurgical and Materials Transactions A. 2004;35:1663–1668.

2. Hao X, Ohtsuka H. Effects of a high magnetic field on transformation temperatures in Fe-based alloys. ISIJ International. 2006;46:1271–1273.

3. Curran D. Dynamic mechanical behavior of iron. In: Shock waves and the mechanical properties of solids. Burke J, Weiss V, editors. Syracuse University Press; 1971. p. 121–138.

4. Andrews D. Equation of state of the alpha and epsilon phases of iron. Journal of the Physics and Chemistry of Solids. 1973;34:825–840.

5. Boettger J, Wallace D. Metastability and dynamics of the shock-induced phase transition in iron. Physical Review B. 1997;55:2840–2849.

6. Barker L, Hollenbach R. Shock wave study of the $\alpha \leftrightarrow \varepsilon$ phase transition in iron. Journal of Applied Physics. 1974;45:4872–4887.

7. Clayton J, Murdoch H, Lloyd J, Magagnosc D, Field D. Modeling magnetic field and strain driven phase transitions and plasticity in ferrous metals. Zeitschrift fur Angewandte Mathematik und Mechanik (ZAMM). 2023; in press: DOI:10.1002/zamm.202200612.

8. Murdoch H, Hernández-Rivera E, Giri A. Modeling magnetically influenced phase transformations in alloys. Metallurgical and Materials Transactions A. 2021;52:2896–2908.

9. Zeng Y, Mittnacht T, Werner W, Du Y, Schneider D, Nestler B. Gibbs energy and phase-field modeling of ferromagnetic ferrite (α)$\rightarrow$ paramagnetic austenite (γ) transformation in Fe–C alloys under an external magnetic field. Acta Materialia. 2022;225:117595.

10. Wang J, Zhang J. A real-space phase field model for the domain evolution of ferromagnetic materials. International Journal of Solids and Structures. 2013;50:3597–3609.

11. Wu HH, Ke Y, Zhu J, Wu Z, Wang XL. Effects of magnetic frequency and the coupled magnetic-mechanical loading on a ferromagnetic shape memory alloy. Journal of Physics D. 2021;54:155301.

12. Ohmer D, Yi M, Gutfleisch O, Xu BX. Phase-field modelling of paramagnetic austenite–ferromagnetic martensite transformation coupled with mechanics and micromagnetics. International Journal of Solids and Structures. 2022;238:111365.

13. Sidhom A, Sayed S, Naga S. The influence of magnetic field on the mechanical properties & microstructure of plain carbon steel. Materials Science and Engineering A. 2017;682:636–639.

14. Xie Z, He M, Xu P, Li Q, Pei C, Xie S, Chen Z. A mechanism study on influence of strong external magnetic field on fracture properties of a ferromagnetic steel. AIP Advances. 2019;9:075219.

15. Molotskii M, Kris R, Fleurov V. Internal friction of dislocations in a magnetic field. Physical Review B. 1995;51:12531.

16. Molotskii M, Fleurov V. Dislocation paths in a magnetic field. Journal of Physical Chemistry B. 2000;104:3812–3816.

17. Kakeshita T, Fukuda T, Takeuchi T. Magneto-mechanical evaluation for twinning plane movement driven by magnetic field in ferromagnetic shape memory alloys. Materials Science and Engineering A. 2006;438:12–17.

18. Maugin G, Fomethe A. On the elastoviscoplasticity of ferromagnetic crystals. International Journal of Engineering Science. 1982;20:885–908.

19. Stringfellow R, Parks D, Olson G. A constitutive model for transformation plasticity accompanying strain-induced martensitic transformations in metastable austenitic steels. Acta Metallurgica et Materialia. 1992;40:1703–1716.

20. Tomita Y, Iwamoto T. Constitutive modeling of TRIP steel and its application to the improvement of mechanical properties. International Journal of Mechanical Sciences. 1995;37:1295–1305.

21. Clayton J, Lloyd J. A dynamic finite-deformation constitutive model for steels undergoing slip, twinning, and phase changes. Journal of Dynamic Behavior of Materials. 2021;7:217–247.

22. Lloyd J, Field D, Magagnosc D, Limmer K, Turnage S, Williams C, Clayton J. Manipulating shock waves with metallurgy. Acta Materialia. 2022;234:118042.

23. Turteltaub S, Suiker A. Transformation-induced plasticity in ferrous alloys. Journal of the Mechanics and Physics of Solids. 2005;53:1747–1788.

24. Clayton J, Lloyd J. Finite strain continuum theory for phase transformations in ferromagnetic elastic-plastic solids. Continuum Mechanics and Thermodynamics. 2022;34:1579–1620.

25. Clayton J, Lloyd J. Numerical models for constitutive behaviors of ferrous metals. DEVCOM Army Research Laboratory; 2023. Report No.: ARL-TR-9776.

26. DeSimone A, James R. A constrained theory of magnetoelasticity. Journal of the Mechanics and Physics of Solids. 2002;50:283–320.

27. Mićunović M. Thermodynamical and self-consistent approach to inelastic ferromagnetic polycrystals. Archives of Mechanics. 2006;58:393–430.

28. Daniel L, Hubert O, Buiron N, Billardon R. Reversible magneto-elastic behavior: a multiscale approach. Journal of the Mechanics and Physics of Solids. 2008;56:1018–1042.

29. Maugin G. Continuum mechanics of electromagnetic solids. North-Holland; 1988.

30. Clayton J. Finsler differential geometry in continuum mechanics: fundamental concepts, history, and renewed application to ferromagnetic solids. Mathematics and Mechanics of Solids. 2022;27:910–949.

31. Maugin G, Eringen A. Deformable magnetically saturated media. I. Field equations. Journal of Mathematical Physics. 1972;13:143–155.

32. Rinaldi C, Brenner H. Body versus surface forces in continuum mechanics: is the Maxwell stress tensor a physically objective Cauchy stress. Physical Review E. 2002;65:036615.

33. Rogovoy A. Formalized approach to construction of the state equations for complex media under finite deformations. Continuum Mechanics and Thermodynamics. 2012;24:81–114.

34. Rogovoy A, Stolbova O. Modeling the magnetic field control of phase transition in ferromagnetic shape memory alloys. International Journal of Plasticity. 2016;85:130–155.

35. Rogovoy A, Stolbova O. Microstructural model of the behavior of a ferroalloy with shape memory in a magnetic field. Mechanics of Advanced Materials and Structures. 2022; in press: DOI:10.1080/15376494.2022.2114046.

36. San Martin D, Van Dijk N, Jimenez-Melero E, Kampert E, Zeitler U, Van der Zwaag S. Real-time martensitic transformation kinetics in maraging steel under high magnetic fields. Materials Science and Engineering A. 2010;527:5241–5245.

37. Lloyd J, Field D, Limmer K. A four parameter hardening model for TWIP and TRIP steels. Materials and Design. 2020;194:108878.

38. Duvall G, Graham R. Phase transitions under shock-wave loading. Reviews of Modern Physics. 1977;49:523–579.

39. Barge N, Boehler R. Effect of non-hydrostaticity on the α-ϵ transition of iron. High Pressure Research. 1990;6:133–140.

40. Ma Y, Selvi E, Levitas V, Hashemi J. Effect of shear strain on the α–ϵ phase transition of iron: a new approach in the rotational diamond anvil cell. Journal of Physics: Condensed Matter. 2006;18:S1075-S1082.

41. Robinson A, Brunner T, Carroll S, Drake R, Garasi C, Gardiner T, Haill T, Hanshaw H, Hensinger D, Labreche D, et al. ALEGRA: an arbitrary Lagrangian-Eulerian multimaterial, multiphysics code. In: Proceedings of the 46th AIAA Aerospace Sciences Meeting; p. AIAA–2008–1235.

42. Noble C, Anderson A, Barton N, Bramwell J, Capps A, Change M, Chou J, Dawson D, Diana E, Dunn T, et al. ALE3D: an arbitrary Lagrangian-Eulerian multi-physics code. Lawrence Livermore National Laboratory (LLNL); 2017. Report No.: LLNL-TR-732040.

43. de Rességuier T, Hallouin M. Effects of the α- ε phase transition on wave propagation and spallation in laser shock-loaded iron. Physical Review B. 2008;77:174107.

44. Grujicic M, Sankaran N. Dispersed-phase martensitic transformation controlled deformation behavior of two-phase metallic materials. International Journal of Solids and Structures. 1997;34:4421–4446.

45. Preston D, Tonks D, Wallace D. Model of plastic deformation for extreme loading conditions. Journal of Applied Physics. 2003;93:211–220.

46. Lloyd J, Clayton J, Becker R, McDowell D. Simulation of shock wave propagation in single crystal and polycrystalline aluminum. International Journal of Plasticity. 2014;60:118–144.

47. Lloyd J, Clayton J, Austin R, McDowell D. Shock compression modeling of metallic single crystals: comparison of finite difference, steady wave, and analytical solutions. Advanced Modeling and Simulation in Engineering Sciences. 2015;2:14.

48. Clayton J. Nonlinear mechanics of crystals. Springer; 2011.

49. Clayton J. Differential geometry and kinematics of continua. World Scientific; 2014.

50. Kocks U. The relation between polycrystal deformation and single-crystal deformation. Metallurgical and Materials Transactions B. 1970;1:1121–1143.

51. Asaro R. Crystal plasticity. Journal of Applied Mechanics. 1983;50:921–934.

52. Clayton J. Defects in nonlinear elastic crystals: differential geometry, finite kinematics, and second-order analytical solutions. Zeitschrift fur Angewandte Mathematik und Mechanik (ZAMM). 2015;95:476–510.

53. Bammann D, Chiesa M, Horstemeyer M, Weingarten L. Failure in ductile materials using finite element methods. In: Structural crashworthiness and failure.

Jones N, Wierzbicki T, editors. Elsevier Applied Science, The Universities Press; 1993. p. 1–54.

54. Simo J, Hughes T. Computational inelasticity. Springer-Verlag; 1998.

55. Nemat-Nasser S. Plasticity: A treatise on finite deformation of heterogeneous inelastic materials. Cambridge University Press; 2004.

56. Hoger A, Carlson D. Determination of the stretch and rotation in the polar decomposition of the deformation gradient. Quarterly of Applied Mathematics. 1984;42:113–117.

57. Miehe C. A constitutive frame of elastoplasticity at large strains based on the notion of a plastic metric. International Journal of Solids and Structures. 1998;35:3859–3897.

58. Miehe C. A formulation of finite elastoplasticity based on dual co-and contravariant eigenvector triads normalized with respect to a plastic metric. Computer Methods in Applied Mechanics and Engineering. 1998;159:223–260.

59. Johnson G, Stryk R, Holmquist T, Beissel S. Numerical algorithms in a Lagrangian hydrocode. Alliant Techsystems Inc.; 1997. Report No.: WL-TR-1997-7039.

60. Cocks A, Ashby M. Intergranular fracture during power-law creep under multiaxial stresses. Metal Science. 1980;14:395–402.

61. Cocks A, Ashby M. On creep fracture by void growth. Progress in Materials Science. 1982;27:189–244.

62. Marin E, McDowell D. Associative versus non-associative porous viscoplasticity based on internal state variable concepts. International Journal of Plasticity. 1996;12:629–669.

63. Soares G, Hokka M. The Taylor–Quinney coefficients and strain hardening of commercially pure titanium, iron, copper, and tin in high rate compression. International Journal of Impact Engineering. 2021;156:103940.

64. Clayton J. Dynamic plasticity and fracture in high density polycrystals: constitutive modeling and numerical simulation. Journal of the Mechanics and Physics of Solids. 2005;53:261–301.

65. Miller M, McDowell D. Modeling large strain multiaxial effects in FCC polycrystals. International Journal of Plasticity. 1996;12:875–902.

66. Kohar C, Cherkaoui M, El Kadiri H, Inal K. Numerical modeling of TRIP steel in axial crashworthiness. International Journal of Plasticity. 2016;84:224–254.

67. Germain P, Suquet P, Nguyen Q. Continuum thermodynamics. ASME Journal of Applied Mechanics. 1983;50:1010–1020.

68. Onsager L. Reciprocal relations in irreversible processes. I. Physical Review. 1931;37:405–426.

69. Ziegler H. Some extremum principles in irreversible thermodynamics with application to continuum mechanics. In: Progress in Solid Mechanics; Vol. 4. Sneddon I, Hill R, editors. North-Holland; 1963. p. 93–193.

70. Hackl K, Fischer F. On the relation between the principle of maximum dissipation and inelastic evolution given by dissipation potentials. Proceedings of the Royal Society A. 2008;464:117–132.

71. Landau L, Lifshitz E, Pitaevskii L. Electrodynamics of continuous media. 2nd ed. Pergamon; 1982.

72. Bancroft D, Peterson E, Minshall S. Polymorphism of iron at high pressure. Journal of Applied Physics. 1956;27:291–298.

73. Marsh SP, editor. LASL shock hugoniot data. University of California Press; 1980.

74. Davison L. Fundamentals of shock wave propagation in solids. Springer; 2008.

75. Clayton J. Nonlinear elastic and inelastic models for shock compression of crystalline solids. Springer; 2019.

76. Clayton J. Nonlinear thermomechanics for analysis of weak shock profile data in ductile polycrystals. Journal of the Mechanics and Physics of Solids. 2019;124:714–757.

77. Clayton J. Analysis of shock compression of strong single crystals with logarithmic thermoelastic-plastic theory. International Journal of Engineering Science. 2014;79:1–20.

List of Symbols, Abbreviations, and Acronyms

TERMS:

2-D	two-dimensional
3-D	three-dimensional
AR	as rolled
ARL	Army Research Laboratory
BCC	body-centered cubic
CMF	constitutive model framework
Cr	chromium
DEVCOM	US Army Combat Capabilities Development Command
EOS	equation of state
FCC	face-centered cubic
Fe	iron
FE	finite element
HCP	hexagonal close-packed
HT	heat treated
Mn	manganese
Ni	nickel
SS	stainless steel
TRIP	transformation-induced plasticity

MATHEMATICAL SYMBOLS:

$\boldsymbol{B}$	magnetic flux density
$\boldsymbol{d}$	deformation rate tensor
$\boldsymbol{F}$	deformation gradient
$\mathbb{G}$	Gibbs free energy per unit reference volume

$\boldsymbol{H}$	magnetic field
$\boldsymbol{J}$	electric current density
$\boldsymbol{l}$	Eulerian velocity gradient
$\boldsymbol{M}$	magnetization per unit spatial volume
p	Cauchy pressure
P	longitudinal shock pressure
t	time
$\boldsymbol{t}$	Cauchy stress tensor
$\boldsymbol{x}$	spatial coordinates
$\boldsymbol{X}$	reference coordinates
ρ	mass density
$\boldsymbol{v}$	particle velocity
τ	shear stress
$\boldsymbol{\omega}$	spin tensor
ξ	transformed phase volume fraction
θ	temperature

1 (PDF) DEFENSE TECHNICAL INFORMATION CTR
DTIC OCA

1 (PDF) DEVCOM ARL
FCDD RLB CI
TECH LIB

1 (PDF) LAWRENCE LIVERMORE NAT LAB
R AUSTIN

1 (PDF) SANDIA NAT LAB
J NIEDERHAUS

1 (PDF) UNIV WISCONSIN
C BRONKHORST

32 (PDF) DEVCOM ARL
FCDD RLA
J CIEZAK
S SCHOENFELD
FCDD RLA B
R BECKER
A TONGE
FCDD RLA HC
J CRONE
J KNAP
FCDD RLA MB
D MAGAGNOSC
G GAZONAS
Z WILSON
FCDD RLA MD
S CLUFF
FCDD RLA MF
D FIELD
C HAINES
K LIMMER
H MURDOCH
FCDD RLA T
M FERMEN-COKER
FCDD RLA TA
M COPPINGER
W UHLIG
C WILLIAMS
FCDD RLA TB
D CASEM
J CLAYTON
B FAGAN
D KRAYTERMAN
J MCDONALD
P MCKEE
C MEREDITH
R REGUEIRO
S SATAPATHY
FCDD RLA TE
J LLOYD
T SCHARF
FCDD RLA TF
J CAZAMIAS
R LEAVY
D MALLICK